Photo-imprint Photoacoustic Microscopy for Three-dimensional Label-free Sub-diffraction Imaging

Junjie Yao, Lidai Wang, Chiye Li, Chi Zhang, Lihong V. Wang[*]

Optical Imaging Laboratory, Department of Biomedical Engineering, Washington University in St. Louis, St. Louis, MO 63130, USA

[*] Correspondence to: lhwang@wustl.edu

Supplementary Materials

Supplementary Note 1. Theory of photo-imprint photoacoustic microscopy (PI-PAM)

Based on the theory of the photoacoustic effect, if the excitation pulse is in both thermal and stress confinement, the PA signal amplitude is given by

$$P \propto \Gamma \eta_{th} \mu_a F .$$ (S1)

Here, P is the signal amplitude detected by the ultrasonic transducer, Γ is the Grueneisen coefficient, and η_{th} is the percentage of the absorbed photon energy that is converted into heat. μ_a is the optical absorption coefficient and F is the optical fluence. Since F is proportional to the excitation intensity I, and μ_a is proportional to the number of molecules N, Eq. S1 can be rewritten as

$$P \propto \Gamma \eta_{th} N I .$$ (S2)

Photobleaching is generally regarded as a stochastic process, where the number of molecules that are bleached by any excitation pulse is proportional to the number of unbleached molecules present at the beginning of this excitation. This type of process can be modeled by an exponential decay function as

$$N_i = N_0 \exp(-\beta i) ,$$ (S3)

where N_i is the number of unbleached molecules after the i th excitation, N_0 is the initial number of molecules, and β denotes the bleaching rate.

Based on the bleaching theory, the bleaching rate has strong dependence on excitation intensity. For most fluorescent materials, the photochemical bleaching rate has an

intensity power dependence of one for one-photo absorption, and at least two for two-photon absorption. For other materials that go through photothermal bleaching, the bleaching rate usually has an intensity power dependence greater than one. Collectively, the bleaching rate can be expressed as

$$\beta = kI^b,\qquad(S4)$$

where k is a constant factor and b is the intensity power dependence with $b \geq 0$.

Substituting Eqs. S3-S4 into Eq. S2, we get

$$P_i \propto \Gamma \eta_{th} N_0 I \exp(-kI^b i).\qquad(S5)$$

The first-order Taylor expansion of Eq. S5 yields

$$P_i \propto \Gamma \eta_{th} N_0 I (1 - kI^b i) = \underbrace{\Gamma \eta_{th} N_0 I}_{\text{Conventional PAM}} - \underbrace{ki\Gamma \eta_{th} N_0 I^{b+1}}_{\text{Photobleaching}}.\qquad(S6)$$

Note that the first part in the right-hand side of Eq. S6 denotes the conventional PAM signal, while the second part denotes the signal decay induced by photobleaching.

The contrast of the PI-PAM comes from the differential signal between adjacent frames, expressed as

$$\Delta P = P_{i-1} - P_i \propto k\Gamma \eta_{th} N_0 I^{b+1}.\qquad(S7)$$

Eq. S7 indicates that, on the one hand, the PI-PAM signal is linear to the optical absorption, which maintains its functional imaging capability, such as oxygen saturation measurement. On the other hand, the PI-PAM signal is nonlinear to the excitation intensity, which enables sub-diffraction imaging capability.

Supplementary Note 2. Effective lateral resolution of PI-PAM

The image resolution is jointly determined by the effective point spread function (PSF) of the excitation volume and the PSF of the detection system. In PA microscopy, since the focused ultrasonic traducer has a focal spot size on the level of tens of micrometers, the imaging resolution is determined predominantly by the excitation PSF. Because PI-PAM is a nonlinear optical measurement, where the differential signal is given by Eq. S7, the effective PSF can be expressed as

$$PSF_r = PSF_r^{\text{excitation}} \times PSF_r^{\text{bleaching}}, \tag{S8}$$

where $PSF_r^{\text{excitation}}$ is the PSF of the excitation volume, and $PSF_r^{\text{bleaching}}$ is the PSF of bleaching profile.

If the excitation profile can be approximated by a Gaussian function, we obtain

$$PSF_r^{\text{excitation}}(r) = \exp(-\frac{2r^2}{w_e^2}) \tag{S9}$$

$$PSF_r^{\text{bleaching}}(r) = \exp(-\frac{2br^2}{w_e^2}), \tag{S10}$$

where r is the radial distance from the center of the Airy disk, and w_e is the Gaussian width of the excitation beam where the beam intensity drops to $1/e^2$ of its center value. The full-width-at-half-maximum (FWHM) of the excitation beam can be expressed as

$$FWHM_r^{\text{excitation}} = \sqrt{2\ln 2}w_e \approx 0.51\frac{\lambda_0}{NA}, \tag{S11}$$

where λ_0 is the excitation wavelength and NA is the numerical aperture of the objective.

Therefore, the effective lateral PSF of the imaging system can be described as

$$PSF_r(r) = \exp(-\frac{2(1+b)r^2}{w_e^2}). \tag{S12}$$

From Eq. S12, we obtain the FWHM of the lateral PSF of the imaging system as

$$FWHM_r = \sqrt{\frac{2\ln 2}{1+b}}w_e \approx \frac{0.51}{\sqrt{1+b}}\frac{\lambda_0}{NA} = \frac{1}{\sqrt{1+b}}FWHM_r^{\text{excitation}}. \tag{S13}$$

Eq. S13 indicates that, compared with conventional PAM, the lateral resolution of PI-PAM has been improved by a factor of $\sqrt{1+b}$.

Supplementary Note 3. Optical sectioning for PI-PAM

Similarly, if we approximate the excitation beam as a Gaussian beam, the axial PSF of PI-PAM for point targets can be expressed as

$$PSF_z^{\text{point}}(z) = [1 + (\frac{z}{z_R})^2]^{-(1+b)}, \tag{S14}$$

where Z_R is the Rayleigh range of the Gaussian beam, which is given by

$$Z_R = \pi \frac{w_e^2}{\lambda_0} \approx 0.9 \frac{\lambda_0}{NA^2}. \tag{S15}$$

The axial resolution of PI-PAM for point targets is then given by the FWHM of the axial PSF as

$$FWHM_z^{\text{point}} = 2\sqrt{2^{1/(1+b)} - 1} z_R = 1.8\sqrt{2^{1/(1+b)} - 1} \frac{\lambda_0}{NA^2}, \tag{S16}$$

which indicates an axial resolution improvement by a factor of $1/\sqrt{2^{1/(1+b)} - 1}$ over conventional PAM for point targets.

For large (or planar) targets, conventional PAM lacks sectioning capability because its axial PSF is constant.

By contrast, for PI-PAM, the axial PSF for planar targets is given by

$$PSF_z^{\text{planar}}(z) = [1 + (\frac{z}{z_R})^2]^{-b}. \tag{S17}$$

Therefore, the optical sectioning capability can be expressed as the FWHM of the axial PSF:

$$FWHM_z^{\text{planar}} = 2\sqrt{2^{1/b} - 1} z_R = 1.8\sqrt{2^{1/b} - 1} \frac{\lambda_0}{NA^2}. \tag{S18}$$

Eq. S18 shows that the optical sectioning capability of PI-PAM also depends on the intensity power dependence of the photobleaching rate. When $b = 0$, PI-PAM reduces to the conventional PAM and has no optical sectioning capability. When $b = 1$, PI-PAM has comparable optical sectioning capability to confocal microscopy.

Supplementary Note 4. Signal-to-noise ratio of PI-PAM

The signal-to-noise ratio (SNR) ultimately determines the detection sensitivity of the system. In PI-PAM, the field of interest is repeatedly scanned to generate a set of M frames $P(i)$, $i = 1 \cdots M$. The detected PA signal P has two contributions:

$$P(i) = s(i) + n(i),\qquad\qquad(S19)$$

where s is the true PA signal and n is the noise, mainly from the electronics. Here, we consider the noise as white noise with a standard deviation of σ.

To a first-order approximation, we assume that the PA signal linearly decays from s_0 to $(1-q)s_0$ within M frames, where q is the bleached percentage with $0 \le q \le 1$. For conventional PAM where the M frames are averaged, the SNR is

$$SNR_{\text{C-PAM}} = \frac{\dfrac{2-q}{2}s_0}{\sigma / \sqrt{M}} = \frac{2-q}{2\sqrt{M}}\frac{s_0}{\sigma}.\qquad\qquad(S20)$$

For PI-PAM, differential signals are first taken between frames that are M/2 apart, and then averaged. The SNR becomes

$$SNR_{\text{PI-PAM}} = \frac{\dfrac{q}{2}s_0}{\sqrt{2}\sigma / \sqrt{M/2}} = \frac{q}{4\sqrt{M}}\frac{s_0}{\sigma}.\qquad\qquad(S21)$$

Therefore, the SNR ratio between PI-PAM and conventional PAM is given by

$$R_{\text{SNR}} = \frac{SNR_{\text{PI-PAM}}}{SNR_{\text{C-PAM}}} = \frac{q}{2(2-q)}.\qquad\qquad(S22)$$

Eq. S22 suggests that the SNR advantage of conventional PAM decreases as the bleached percentage q increases. For example, in the case where the signal has decayed to half of the initial value ($q = 0.5$), the expected SNR difference is 6 times.

Supplementary methods:

1. Experimental setup of PI-PAM

As shown in Supplementary Fig. 1, our PI-PAM is implemented in transmission mode. An integrated diode-pumped Q-switched laser and optical parametric oscillator system (NT242-SH, Ekspla Inc.) generate laser pulses (5 ns pulse width, 1 KHz repetition rate) with a tunable wavelength range from 210 to 2600 nm. The laser pulses are sequentially filtered by an iris (2 mm aperture), focused by a condenser lens, filtered by a 50 μm pinhole, and focused again by an objective. This oil-immersion objective for visible light (MPlanApoN100XO, Olympus Inc.) has a 1.4 numerical aperture (NA). A beam sampler reflects a small portion of the excitation beam to a high-sensitivity photodiode, which records the pulse-by-pulse laser intensity. The photoacoustic waves are detected by a focused ultrasonic transducer (customized with 40 MHz central frequency, 80% bandwidth, and 0.50 NA), which is placed confocally with the objective and coupled by water. The received PA signal is then amplified by 48 dB through a low-noise wide-band amplifier, digitized at a 1 GHz sampling rate (PCI-5152, National Instruments Inc.), and finally recorded by a computer. The relative optical absorption is calculated by the amplitude of the photoacoustic signals. The arrival time of each photoacoustic signal is converted to depth through the speed of sound in water (1500 m/s at room temperature). Three-dimensional imaging is realized by scanning the sample by a high-precision scanning stage (PLS85, Micos Inc.). A customized synchronizing controller sends out trigger signals for the laser firing, data acquisition, and motor scanning. A customized Labview program synchronizes the entire system. PI-PAM imaging can be performed point by point (A-scan mode), cross-section by cross-section (B-scan mode), or volume by volume (C-scan mode). If not otherwise mentioned, A-scan mode was used for the experiments in this paper. To achieve sufficient detection sensitivity, typically more than 200 frames were acquired for each experiment.

2. Data processing

The recorded raw PA signal was first compensated for by the excitation intensity measured by the photodiode. Each A-line signal was then Hilbert transformed. The

amplitude of the transformed signal was extracted and used for further analysis. Theoretically, the differential analysis can be performed between adjacent frames. However, for slow bleaching samples, the signal difference between adjacent frames is comparable with the noise level. To improve the signal-to-noise ratio (SNR), in practice, we took the difference between frames that are half of the total frames apart, and then averaged all the differential images. This method can improve the SNR as shown below.

Assume that the total number of frames is M, the true signal difference between adjacent frames is ΔS, and the standard deviation of the white noise is σ. Approximately, averaging of the differential signals between adjacent frames gives an SNR of

$$SNR_1 = \sqrt{\frac{M-1}{2}} \frac{\Delta S}{\sigma}, \tag{S23}$$

while averaging of the differential signals between frames that are $M/2$ apart yields an SNR of

$$SNR_{M/2} = \frac{M}{4} \sqrt{M} \frac{\Delta S}{\sigma}. \tag{S24}$$

Eqs. (S23-24) suggest that an SNR improvement of $M/2\sqrt{2}$ can be achieved.

Supplementary Figures and captions
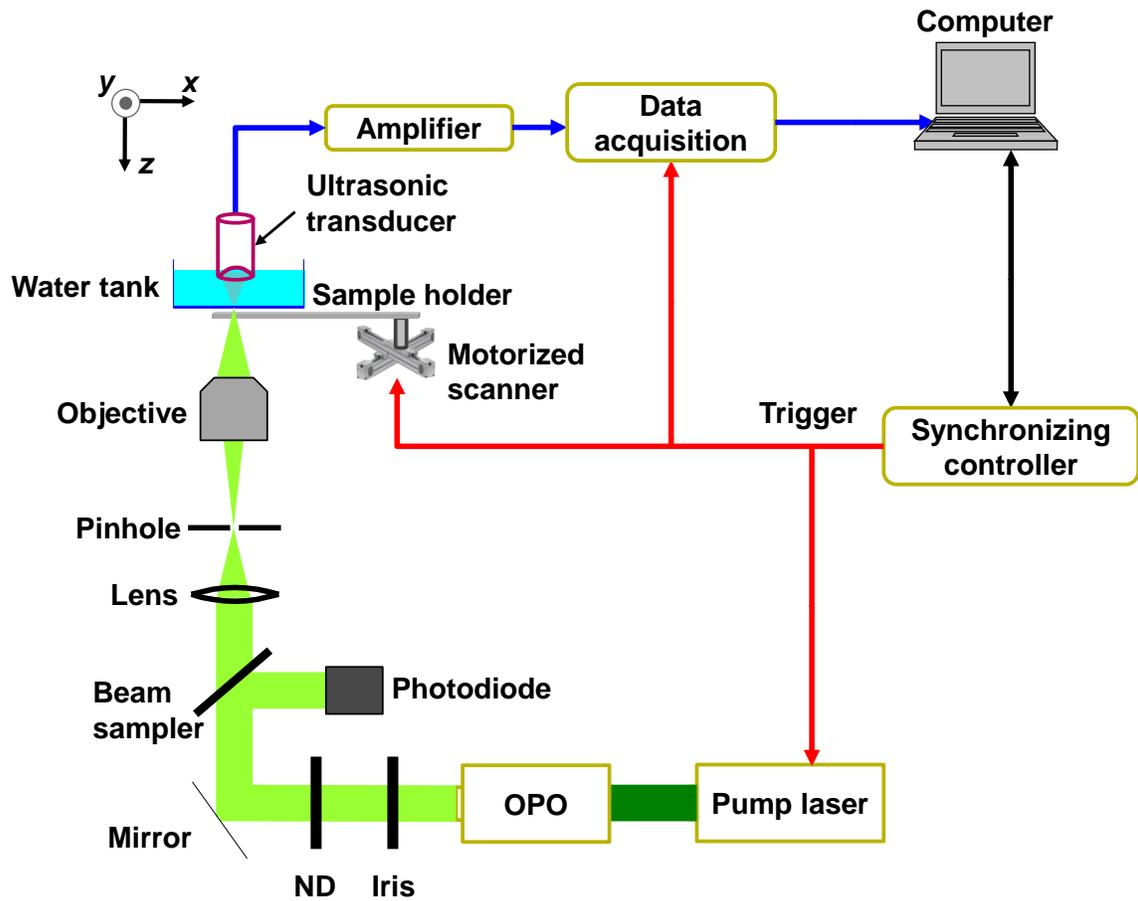
Supplementary Fig. 1. Schematic of PI-PAM. An integrated diode-pumped Q-switched laser and optical parametric oscillator system generate laser pulses with a tunable wavelength range from 210 to 2600 nm. The filtered laser pulses are focused by an oil-immersion objective. The resultant photoacoustic waves are detected by a focused ultrasonic transducer, which is placed confocally with the objective and coupled by water. The received PA signal is amplified, digitized, and finally recorded by a computer. A customized Labview program synchronizes the entire system. ND, neutral density filter; OPO, optical parametric oscillator.
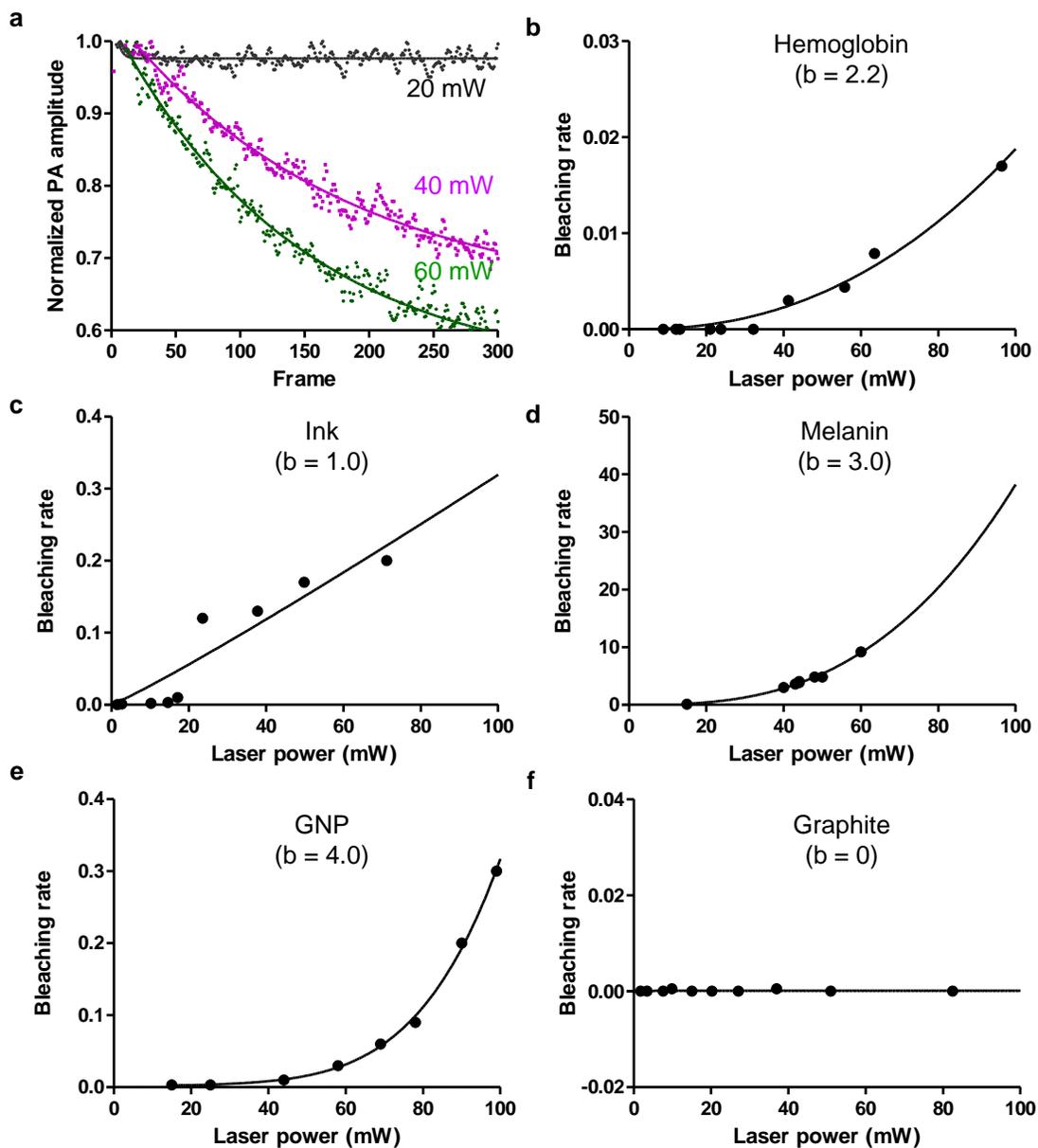
Supplementary Fig. 2. Photobleaching characteristics of several common materials. (a) The photoacoustic signal amplitude of hemoglobin decays with the number of laser pulse excitations. Higher laser power yields a greater decay rate. (b-f) Photobleaching rates of different materials have different intensity power dependences. GNP, gold nanoparticle. b: power dependence of the photobleaching rate on the excitation intensity.
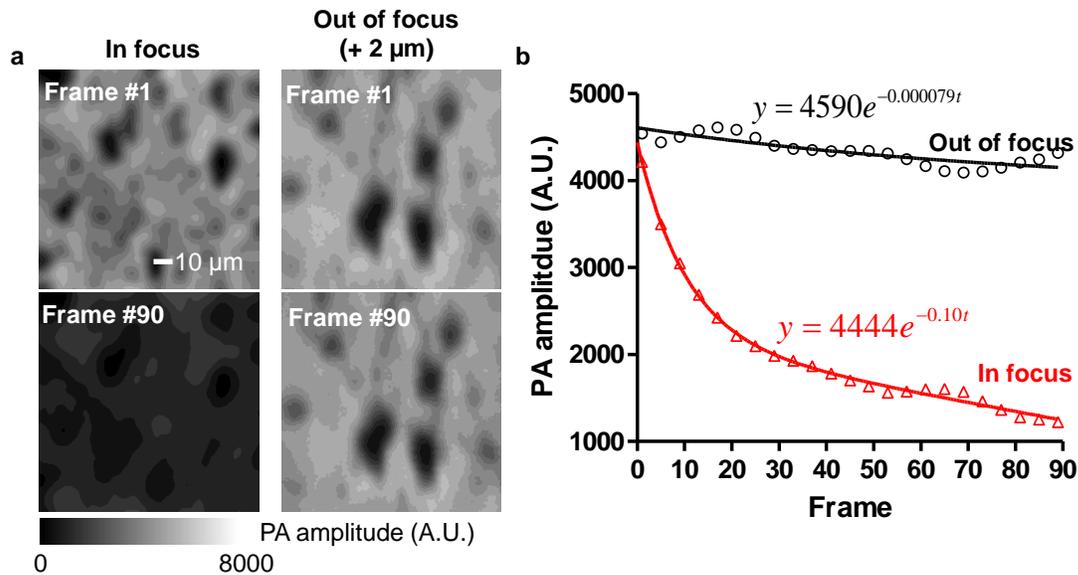
Supplementary Fig. 3. Photobleaching rate of thin-layer hemoglobin in- and out-of-focus. (a) PAM images of the thin-layer hemoglobin before and after bleaching when the sample is in-focus (left) and 2 µm out-of-focus (right). (b) Quantitative analysis of the signal decay when the sample is in- and out-of-focus. The exponential fitting shows that the in-focus decay rate is about 15 times greater than the out-of-focus rate. Note that before the bleaching, the in- and out-of-focus signals have similar strength, which shows that conventional PAM does not have sectioning capability.

a

b　White light

**c**　Fluorescence

— 10 µm

— 10 µm
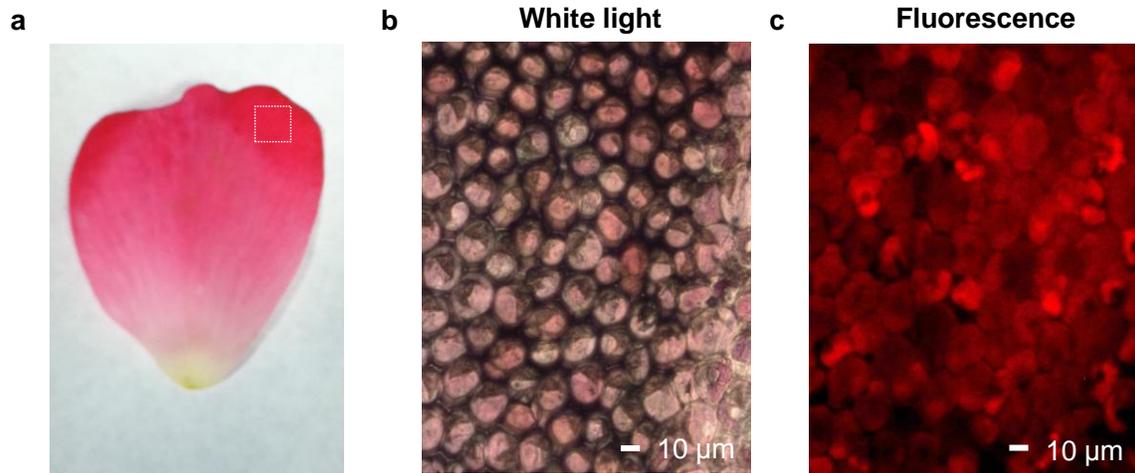
Supplementary Fig. 4. Wide-field optical microscopy of rose petal epidermal cells. (a) The epidermal layer of a freshly harvested rose petal was washed and carefully peeled off for wide-field optical microscope imaging. (b) Wide-field optical microscopy of the epidermal cells under white light. The pinkish parts are cell vacuoles. (c) Wide-field fluorescence microscopy of the same region as (b), where the vacuoles show bright fluorescence and the cell walls and nuclei are dark.
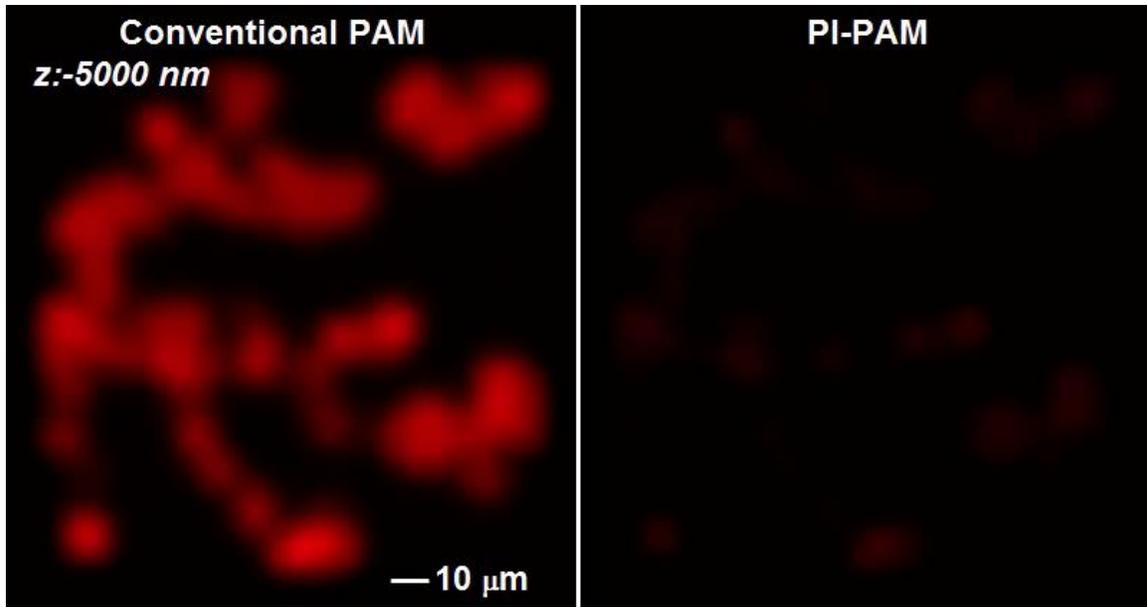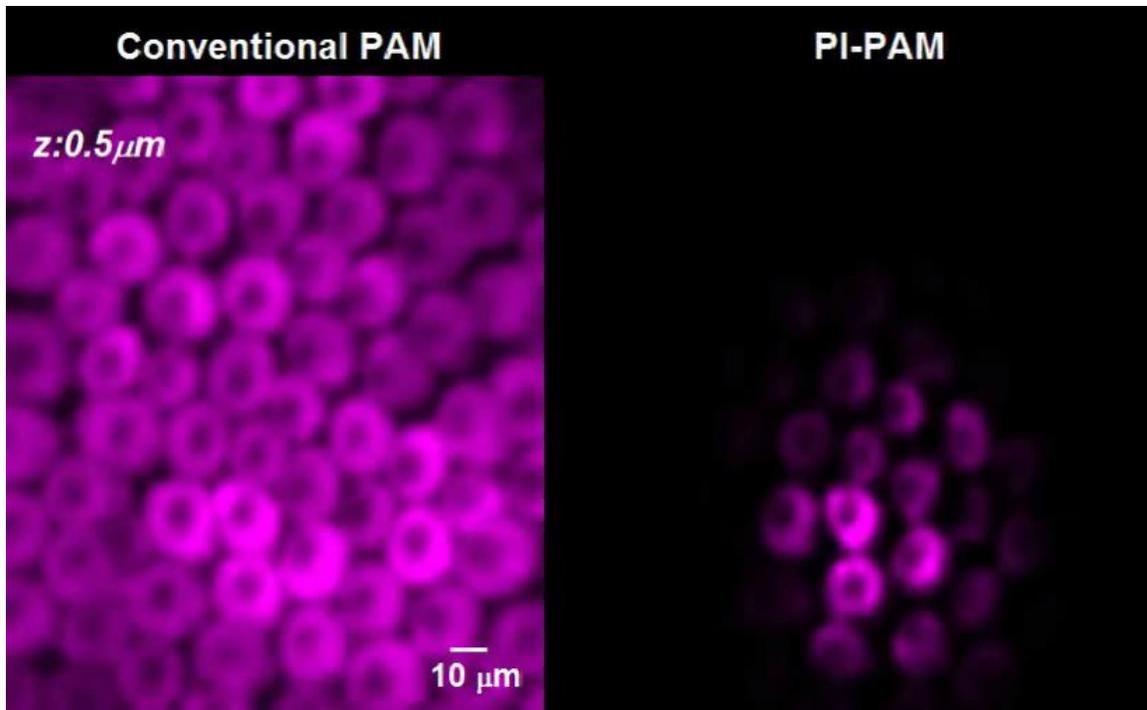
Movies captions
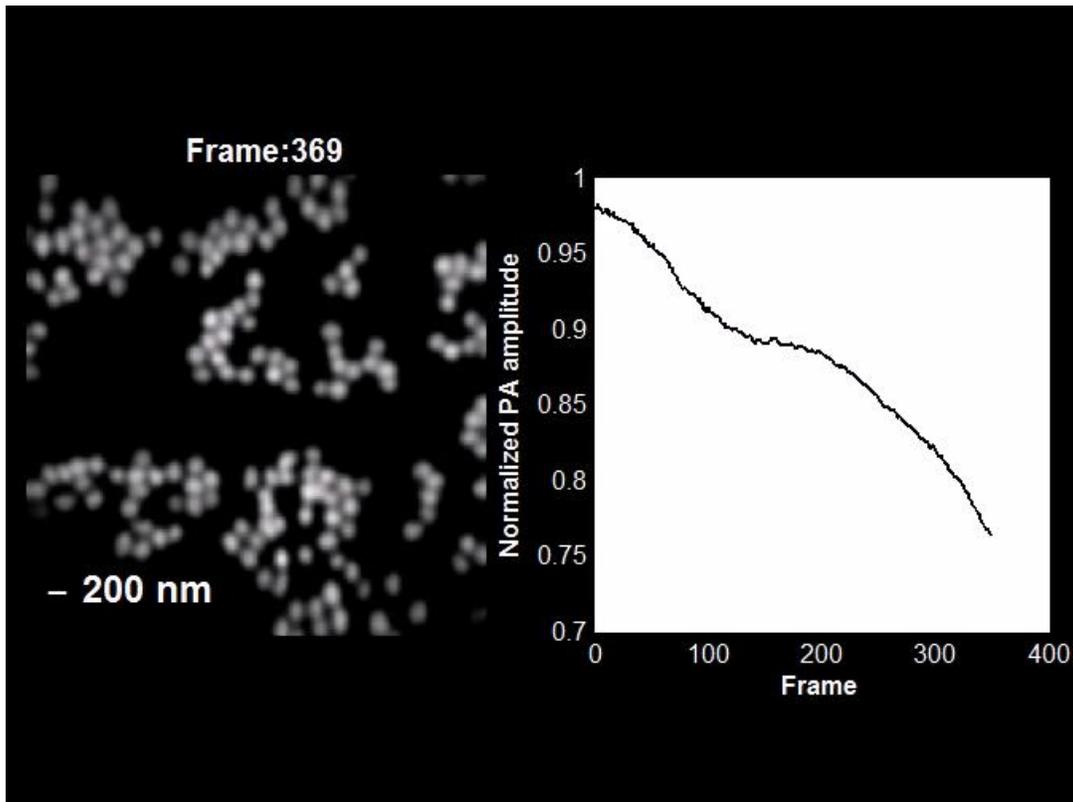
Movie S1. The photobleaching time course of 150-nm-diameter gold nanoparticles imaged by PI-PAM.
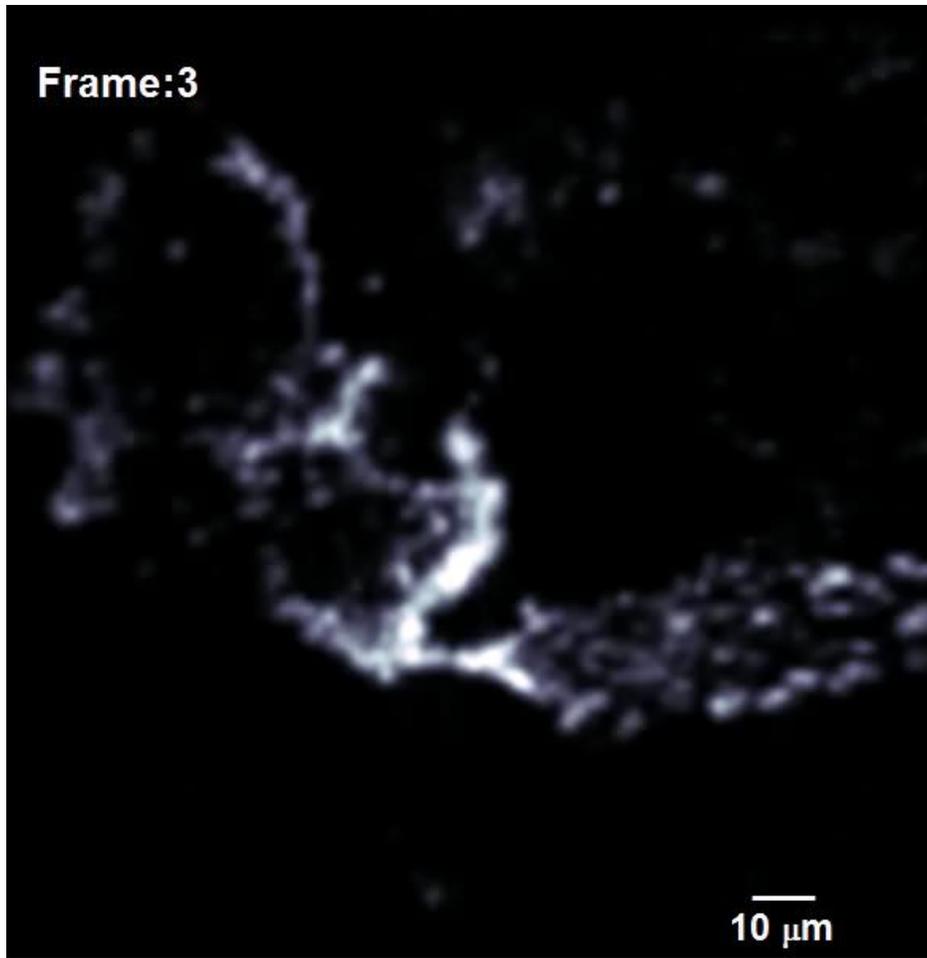
Movie S2. The photobleaching time course of a B16 melanoma cell imaged by PI-PAM.

Movie S3. Conventional PAM and PI-PAM images of a single layer of red blood cells acquired at axial positions ranging from -5 µm to +5 µm.

Movie S4. Optical sectioning of rose petal epidermal cells by conventional PAM and PI-PAM.